View metadata, citation and similar papers at core.ac.uk

brought to you by CORE

provided by NASA Technical Reports Server

NASA TECHNICAL NOTE

NASA TN D-8377

NASA TN D-8377
C.1

COPY: RET
AFWL TECHNICAL
KIRTLAND AFB,

TECH LIBRARY KAFB, NM
0134097

SIGNAL-TO-NOISE RATIO ANALYSIS AND EVALUATION OF THE HADAMARD IMAGING TECHNIQUE

Daniel J. Jobson, Stephen J. Katzberg, and Robert B. Spiers, Jr.

Langley Research Center
Hampton, Va. 23665

NATIONAL AERONAUTICS AND SPACE ADMINISTRATION • WASHINGTON, D. C. • MARCH 1977

TECH LIBRARY KAFB, NM
0134097

1. Report No.	2. Government Accession No.	
NASA TN D-8377		

4. Title and Subtitle	5. Report Date
SIGNAL-TO-NOISE RATIO ANALYSIS AND EVALUATION OF THE HADAMARD IMAGING TECHNIQUE	March 1977
	6. Performing Organization Code
7. Author(s)	8. Performing Organization Report No.
Daniel J. Jobson, Stephen J. Katzberg, and Robert B. Spiers, Jr.	L-11042
9. Performing Organization Name and Address	10. Work Unit No.
NASA Langley Research Center Hampton, VA 23665	176-30-31-09
	11. Contract or Grant No.
	13. Type of Report and Period Covered
12. Sponsoring Agency Name and Address	Technical Note
National Aeronautics and Space Administration Washington, DC 20546	14. Sponsoring Agency Code

15. Supplementary Notes

16. Abstract

The Hadamard imaging technique, using binary coded masks to scan image space mechanically, enables large numbers of image elements to be sampled simultaneously, in contrast to the sequential sampling of conventional imaging. This technique was originally used to improve the signal-to-noise ratio performance of grating spectrometers. An analogous performance advantage when applied to imaging has not been verified. This paper analyzes the signal-to-noise ratio performance of the Hadamard imaging technique and presents an experimental evaluation of a laboratory Hadamard imager. A comparison between the performances of Hadamard and conventional imaging techniques shows that the Hadamard technique is superior only when the imaging objective lens is required to have an effective F number of about 2 or slower.

17. Key Words (Suggested by Author(s))	18. Distribution Statement
Hadamard Hadamard imaging Hadamard performance evaluation Performance comparison Imaging	Unclassified - Unlimited Subject Category 35

19. Security Classif. (of this report)	20. Security Classif. (of this page)	21. No. of Pages	22. Price*
Unclassified	Unclassified	30	$3.75

* For sale by the National Technical Information Service, Springfield, Virginia 22161

SIGNAL-TO-NOISE RATIO ANALYSIS AND EVALUATION OF THE HADAMARD IMAGING TECHNIQUE

Daniel J. Jobson, Stephen J. Katzberg,
and Robert B. Spiers, Jr.
Langley Research Center

SUMMARY

The Hadamard imaging technique, using binary coded masks to scan image space mechanically, enables large numbers of image elements to be sampled simultaneously, in contrast to the sequential sampling of conventional imaging. This technique was originally used to improve the signal-to-noise ratio performance of grating spectrometers. An analogous performance advantage when applied to imaging has not been verified. This paper analyzes the signal-to-noise ratio performance of the Hadamard imaging technique and presents an experimental evaluation of a laboratory Hadamard imager. A comparison between the performances of Hadamard and conventional imaging techniques shows that the Hadamard technique is superior only when the imaging objective lens is required to have an effective F number of about 2 or slower.

INTRODUCTION

Electro-optical imagers used in most applications have measured the radiance distribution of a scene either by mechanically scanning an image across the active area of a single photodetector or by electronically scanning a stationary image with a detector array. In both types of imagers, elements of the image are sampled sequentially. An imaging technique which uses binary coded masks to sample large numbers of image elements simultaneously has been suggested. (See ref. 1.)

This imaging technique uses masks with patterns of opaque and transparent elements arranged according to a predetermined binary code to scan a stationary image mechanically. The motion of the mask causes different combinations of image elements to be transmitted to a photodetector which responds with an electrical signal proportional to the sum of the transmitted elements. An image is recovered from this series of electrical signals when the solution of the set of equations which mathematically represents the measurement process is computed.

One binary code particularly useful as a mask pattern is a cyclical modified Hadamard code. This code is selected for reasons of compactness, ease of data reduction, and unbiased efficient sampling. Cyclical codes eliminate the need for a unique mask pattern for each successive sample of the electronic signal. The use of Hadamard codes allows simple fast recovery of image data from the electronic signals because the solution of the set of equations requires a simple matrix inversion. In addition, the use of Hadamard codes

provides unbiased efficient sampling since each image element appears in about one-half of the summations. (See ref. 2.)

Although the use of Hadamard masks in grating spectrometers provides improved signal-to-noise ratio performance in comparison with conventional scanning, there is no experimental verification that a Hadamard imager can achieve analogous gains in performance when compared with conventional imaging methods. In fact, one paper in the literature has expressed doubt that substantial improvements can be achieved. (See ref. 3.)

A general analysis of the signal-to-noise ratio performance of the Hadamard imaging technique is given here. In addition, an analysis and the results of performance measurements of a laboratory Hadamard imager are presented. The results of the analyses and measurements are used to draw a comparison of the Hadamard and conventional imaging techniques.

SYMBOLS

$A_{i,j}$	Hadamard code elements arranged to represent imaging process
A_o	objective lens aperture area, m^2
a	detector area, m^2
C,C'	empirical constants for "1/f" noise
c	proportionality constant, $V/m\text{-}Hz^{1/2}$
D	lens aperture diameter or length of one side of square aperture, m
d	image diameter, m
d'	image diameter using immersion lens, m
d_p	depth of photoconductor, m
E	electric field, V/m
F	focal length, m
F#	effective F number (F# = ℓ/D)
f	frequency, Hz
G	electronic gain
G'	system electronic gain exclusive of photoconductor and preamplifier
G_p	photoconductor gain
H_e	height of mask code element, m

h	Planck constant
I	spectral irradiance on photoconductor, $W/m^2-\mu m$
i	current, A
i'	photo-induced current, A
i_{NT}	total noise current, A
K	equivalent input noise voltage, V
k	Boltzmann constant
k_s	system constant, $\frac{V}{W/m^2-sr}$
L	focused object distance, m
l	focused lens to image distance, m
ℓ	length between photoconductor electrodes, m
m	number of scene elements
N_j	radiance of jth scene element, W/m^2-sr
$\bar{N}_j$	spectral weighted average radiance of jth scene element, W/m^2-sr
NER	noise equivalent radiance, W/m^2-sr
n	index of refraction
n'	volume density of photogenerated charge carriers, m^{-2}
n_i	noise voltage in ith electronic signal, V
n_t'	total volume density of charge carriers, m^{-2}
PR	performance ratio of Hadamard imager to conventional imager
p	number of samples
q	charge of electron, C
R_1, R_2, R_B	various circuit resistances, ohms
$R(\lambda)$	photoconductor responsivity, V/W
S_i, S_j	ith,jth electronic signal, V

s_j	electronic signal due to jth image element, V
T	temperature, K
t_p	lifetime of charge carriers in photoconductor, sec
V_{BB}	bias voltage, V
V_o	output voltage, V
v_{NA}	preamplifier equivalent input noise voltage, $V/Hz^{1/2}$
v_{Nf}	noise voltage due to feedback resistor, $V/Hz^{1/2}$
v_{NT}	total preamplifier equivalent output noise voltage, $V/Hz^{1/2}$
v_{N1}, v_{N2}, v_{NB}	noise voltages due to various circuit resistors, $V/Hz^{1/2}$
W	electronic bandwidth, Hz
W_e	width of mask code element, m
w	width of photoconductor, m
x	distance from Hadamard mask to field stop along optical axis, m (see fig. 2)
y	distance from field stop to field lens measured along optical axis, m (see fig. 2)
$\alpha(\lambda)$	quantum efficiency of photoconductor, electron-hole pairs/photon
ε	error signal, V
λ	wavelength, μm
μ	mobility of charge carriers, $m^2/V\text{-sec}$
ν	optical frequency, Hz
ξ_λ	photoconductor resistance, ohms
τ	wavelength independent transmissivity of optics
$\tau(\lambda)$	spectral transmissivity of optics
Φ_λ	photons per second arriving at photoconductor per unit wavelength, $(\mu m\text{-sec})^{-1}$
Ω	image element solid angle, sr

Subscripts:

c	conventional imager
F	field lens
H	Hadamard imager
i,j,k	integers
o	objective lens
rms	root mean square

An estimate is denoted by $\langle\ \rangle$. A bar over a symbol indicates the average of the parameter.

THEORETICAL COMPARISON OF CONVENTIONAL AND HADAMARD IMAGING TECHNIQUES

The signal-to-noise ratio performance of both conventional and Hadamard imaging has been investigated to provide a basis for comparison between the two methods. Noise equivalent radiance was chosen as the figure of merit for the comparison. The dominant noise was assumed to be a detector noise which is signal and frequency independent. Performance parameters which may differ in the two cases are subscripted as c for conventional and H for Hadamard.

Conventional Imager

For a conventional imager (see fig. 1), the electronic signal after amplification is related to the radiance of the jth scene element by

$$S_j = A_o \Omega G \int_{\lambda_1}^{\lambda_2} N_j(\lambda)\ \tau_c(\lambda)\ R(\lambda)\ d\lambda + n_j \tag{1}$$

where A_o is the aperture area of the objective lens; Ω, the solid angle subtended by a detector with respect to the objective lens; G, electronic gain; $N_j(\lambda)$, the spectral radiance elements of the scene; $\tau_c(\lambda)$, the spectral transmissivity of the conventional imager optics; $R(\lambda)$, the spectral responsivity of the detector; and n_j, the noise voltage occurring in the jth measurement of S.

A spectrally weighted average radiance is defined as

$$\bar{N}_j = \frac{\int_{\lambda_1}^{\lambda_2} N_j(\lambda)\ \tau_c(\lambda)\ R(\lambda)\ d\lambda}{\int_{\lambda_1}^{\lambda_2} \tau_c(\lambda)\ R(\lambda)\ d\lambda} \tag{2}$$

An estimate of this average is obtained from equations (1) and (2):

$$\langle \bar{N}_j \rangle = \frac{S_j - n_j}{GA_o \Omega I_c} \tag{3}$$

where

$$I_c = \int_{\lambda_1}^{\lambda_2} \tau_c(\lambda)\, R(\lambda)\, d\lambda$$

The noise equivalent radiance or root-mean-square (rms) error in estimating $\bar{N}_j$ from p measurements of each is

$$\left[\frac{\sum_{k=1}^{p} \left(\bar{N}_j - \langle \bar{N}_{j,k} \rangle\right)^2}{p}\right]^{1/2} = \left(\frac{\sum_{k=1}^{p} n_{j,k}^2}{p}\right)^{1/2} \Big/ GA_o \Omega I_c \tag{4a}$$

or

$$(NER)_{j,c} = n_{j,rms} / GA_o \Omega I_c \tag{4b}$$

where $n_{j,rms} = c(a_c W)^{1/2}$ for most detectors, c being some proportionality constant, a_c the detector area, and W the electronic bandwidth.

Hadamard Imager

For Hadamard imaging, a rotating mask is placed in the image plane of an objective lens. (See fig. 2.) A field stop defines the image field, and a field lens condenses the radiant power transmitted by the mask on to a detector. This imaging process is represented in simplified form as

$$S_i = k_s \sum_{j=1}^{m} A_{i,j} N_j \tag{5a}$$

without the presence of noise, or in matrix form

$$[S] = k_s [A][N] \tag{5b}$$

where S_i is the column matrix of electronic signals from the detector, k_s is a system constant, N_j is the column matrix of scene radiance elements, and m is the number of elements in the Hadamard code (as well as the upper limit for i and j). $A_{i,j}$ is an $m \times m$ binary matrix whose first row $A_{1,j}$ is the Hadamard code, each successive row being the previous row cycled by one code element. After m samples of S_i have been taken, a set of m equations in m unknowns has been formed.

To recover the scene radiance distribution, the matrix equation (5b) is solved for [N]

$$[N] = k_s^{-1}[A]^{-1}[S] \tag{6}$$

where $[A]^{-1}$ is a matrix inverse.

The noise equivalent radiance for the Hadamard imager is determined by expanding equations (5b) and (6) to include: (1) the parameters which comprise the system response to radiance, (2) the spectral characteristics of the scene radiance and electro-optical system, and (3) the effect of detector noise. The inclusion of these factors in the summation form of equation (1) yields

$$S_i = A_o \Omega G \sum_{j=1}^{m} A_{i,j} \int_{\lambda_1}^{\lambda_2} N_j(\lambda)\, \tau_H(\lambda)\, R(\lambda)\, d\lambda + n_i \tag{7a}$$

where Ω is now the solid angle subtended by each mask code element. It is often more convenient in practice to use an equivalent form of equation (7a) such as

$$S_i = \sum_{j=1}^{m} A_{i,j} s_j + n_i \tag{7b}$$

where

$$s_j = A_o \Omega G \int_{\lambda_1}^{\lambda_2} N_j(\lambda)\, \tau_H(\lambda)\, R(\lambda)\, d\lambda$$

(that is, the signal contribution of the jth image element). Returning to the matrix form of this equation and letting $I_H = \int_{\lambda_1}^{\lambda_2} \tau_H(\lambda)\, R(\lambda)\, d\lambda$ and $\bar{N}_j$ be defined as before

$$[S] = A_o \Omega G I_H [A][N] + [n] \tag{7c}$$

An estimate of the radiance is then

$$\left[\langle \bar{N} \rangle\right] = \frac{[A]^{-1}([S] - [n])}{A_o \Omega G I_H} \tag{8}$$

and the error in this estimate is

$$\left[\bar{N} - \langle \bar{N} \rangle\right] = \frac{[A]^{-1}[n]}{A_o \Omega G I_H} \tag{9}$$

The root-mean-square value of $[A]^{-1}[n]$ is derived in reference 3 as $\frac{2m^{1/2} n_{i,rms}}{m + 1}$ and gives

$$(NER)_{i,H} = \frac{2m^{1/2}}{m + 1} \frac{n_{i,rms}}{A_o \Omega G I_H} \tag{10}$$

Comparison

Because of the difference in the two types of imaging systems, two parameters in the NER expressions may not be the same for the two cases. These are optical system transmissivity and detector area. For this comparison, the Hadamard imager optical system is assumed to differ from that of the conventional imager only by the addition of a field lens and the deletion of a scan mirror. In addition, the detector areas are likely to be different because for Hadamard imaging the detector area does not have to match the image element area. In fact, the use of a small detector area is difficult to realize in actual hardware. After these considerations have been accounted for, the performance ratio PR of the Hadamard imager to the conventional imager from equations (4b) and (10) (assuming $(NER)_i = NER$, $\tau_c(\lambda) = \tau_c$, and $\tau_H(\lambda) = \tau_H$) becomes

$$PR = \frac{(NER)_c}{(NER)_H} \approx \frac{\tau_H (a_c)^{1/2} (m + 1)}{\tau_c (a_H)^{1/2} (2m^{1/2})} \tag{11a}$$

Because m is usually a large number for most imaging systems, a very close approximation is

$$PR \approx \frac{\tau_H (a_c)^{1/2} m^{1/2}}{\tau_c (a_H)^{1/2} 2} \tag{11b}$$

Since the transmissivities of the optics of the Hadamard and conventional imager systems should not differ greatly, the ratio of the detector areas is of primary concern. Equation (11b) shows that the performance advantage gained by simultaneous sampling of image elements (the $m^{1/2}/2$ factor) is realized only to the extent that the Hadamard imager detector area is made to approach that of a conventional imager. This condition requires demagnifying the total image field to as small an area as possible. First, use of a field lens is assumed to condense radiation on to the detector. Then the minimum detector area, determined from the relationship of object to image size for the field lens (see fig. 2), yields a minimum image diameter of

$$d_H = \frac{D_o l_F}{L_F} \tag{12}$$

Since

$$(a_c)^{1/2} = \frac{\pi^{1/2} d_c}{2}$$

and

$$(a_H)^{1/2} = \frac{\pi^{1/2} d_H}{2}$$

for circular detectors,

$$PR \approx \frac{\tau_H d_c m^{1/2}}{2\tau_c D_o l_F / L_F} \tag{13a}$$

But the image field stop is also the field-lens aperture and gives $D_F = d_c m^{1/2}$, and since the field lens images the objective lens on to the detector, $L_F = l_o + x + y$ results. (See fig. 2.) Thus,

$$PR \approx \frac{\tau_H}{2\tau_c} \left(\frac{l_o + x + y}{D_o} \Big/ \frac{l_F}{D_F} \right) \tag{13b}$$

or with $x + y \ll l_o$ and effective F number defined as $F\# = l/D$, the performance ratio becomes

$$PR \approx \frac{\tau_H}{2\tau_c} \frac{F\#_o}{F\#_F} \tag{13c}$$

This expression illustrates that relative performance of Hadamard imaging is not $m^{1/2}/2$ in practice. Rather, the performance advantage is a much smaller value $\left(F\#_o/F\#_F\right)$ because the Hadamard imager cannot usually be made to have a detector area as small as that of the conventional imager.

Although the Hadamard imager optics include an immersion lens, the conventional imager can also use an immersion lens with the same relative reduction in detector area. This effect would then cancel in the performance ratio. The minimum possible detector area and highest performance ratio are achieved by using the lowest effective F number possible for the field lens.

EXPERIMENTAL EVALUATION OF A HADAMARD IMAGER

System Description

The Hadamard imager which was used as a test instrument is shown in figure 3. This instrument operates in the thermal infrared spectral range from 8 to 14 μm. Figure 2 presents a schematic drawing of the germanium optical subsystem; figure 4 presents a block diagram of the electronics subsystem. Table I summarizes the imager design parameters.

The optical subsystem consists of objective lens, the Hadamard encoding mask, a field lens, and an immersion lens mounted directly on the liquid-nitrogen cooled mercury cadmium telluride (HCT) detector. An image of the scene is formed by the objective lens on the encoding mask. The field stop limits the area of the encoding mask which can transmit radiation from image elements to the remainder of the optical subsystem. Since the field lens images the objective lens on to the detector active area, an out-of-focus image of the encoding mask superimposed on the image field is formed at the detector. Thus, the effect of the field lens is to mix the radiation from the transmitted image elements on to the detector active area. The immersion lens is used to reduce the required active area of the detector to minimize detector noise. An ac motor rotates the mask at 720 revolutions per minute (rpm). This rotation requires the detector signal to be sampled in 25-μsec intervals. A frame of image data is acquired in 25.6 msec. The Hadamard mask contains timing slots to synchronize detector signal sampling with mask rotation. These timing slots are used to create timing pulses by means of small tungsten lights and detectors on opposite sides of the mask.

The electronics subsystem performs signal sampling, integration, amplification, and digitization. (See fig. 4.) In order to realize detector noise-limited performance, the rest of the electronics subsystem should introduce no

appreciable noise. Therefore, the analysis of the electronics subsystem centers on noise sources.

Optical Subsystem

Optics.- A detailed optical arrangement of the Hadamard transform imager is shown in figure 2. The objective lens of focal length F_o forms an image of some object on a digitally encoded field mask. The image frame area is defined by a field-stop aperture placed as close as practical behind the mask at some distance x. This square aperture transmits image radiation which corresponds to a mask area containing 31 by 33 elements.

Upon passing through the field-stop aperture, the radiation is incident on a field lens placed a distance y immediately after the aperture. The best imager signal-to-noise ratio is realized when the field lens concentrates all the encoded radiation on a detector of the smallest size possible. The minimum image size the field lens can form is proportional to the ratio of the image distance l_F and the object lens distance L_F. Therefore, the smallest ratio will be obtained by using the shortest focal length or lowest F number lens. The lowest effective F number possible with refractive optics is 0.5. However, when refractive optics have F numbers less than 1.0, lens aberrations begin to negate any further size reduction. For this imager, an effective F/1.38 lens was selected.

The image diameter d is reduced further to allow a smaller detector size by using hemispherical immersion optics. When the detector is placed in optical contact with the flat back surface of a hemispherical lens of index of refraction n, the image diameter d can be reduced in size to

$$d_H' = \frac{d_H}{n} \tag{14}$$

Therefore, the higher the index of refraction of the immersion lens, the smaller d_H can be made. In this imager, the immersion lens is germanium which has an index of 4 at a 10-μm wavelength; therefore, the image diameter is reduced by 4. In order for the detector to be filled with radiation, the square detector diagonal $W\sqrt{2}$ is made equal to d_H.

Mask.- The coded mask consists of two arc sector areas placed diametrically opposite each other on a rotatable disk as shown in figure 5. The sectors are concentric with the rotation axis of the disk; the sector areas are centered and normal to the optical axis of the objective lens. Therefore, the sector areas are irradiated by the image alternately as the disk rotates. The sector areas are made of thin opaque metallic plates which have small elemental areas chemically etched away in the form of a binary code. The transparent and opaque elemental areas are effectively square in shape with a width W_e and height H_e. These elemental areas are arranged in 31 concentric rows. Each row contains 1088 elements, 65 of which are redundant. The other sector area is arranged identically. The modified Hadamard code given in reference 3 determines which elements are opaque and which are transparent. Two image

frames of information are presented for processing with each rotation of the mask disk. The elemental solid angular field of view (in steradians) of the imager is given by

$$\Omega = \frac{W_e H_e}{\ell_o^2} \tag{15}$$

Electronics Subsystem

This section reviews the basic performance of the radiation detector, presents an analysis of the succeeding preamplification and video processing, and compares those predictions with actual system measurements.

Detector.- The detector used in this system is a commercial mercury cadmium telluride (HCT) detector optimized for operation from approximately 8 to 14 μm. Resistances of these detectors are a function of their temperature, field of view, and the object radiance. In the configuration used in this study the HCT is enclosed in a Dewar which maintains a detector temperature of 77 K and restricts detectable energy to a 60° field of view. Detector size is 2.5 mm by 2.5 mm, and it is directly bonded to a germanium immersion lens. The HCT used in this application operates in the photoconductive mode and has approximately 40 ohms of element resistance when viewing a 295-K field.

Photoconductors such as the HCT very nearly approach background photon noise-limited performance at their peak wavelength. The basic photoconductor noise mechanisms are a "1/f" noise arising from contacts, generation-recombination noise (G-R), arising from random creation and removal of carriers from the conduction process, and finally, Johnson noise arising from the random motion of the free carriers themselves. (See ref. 4.) To put this discussion in more quantitative terms, the situation illustrated in figure 6 is used as the basis for a model of the photon detector and noise processes. The detector has a bias current impressed upon it and is assumed to be receiving a spectral irradiance I_λ in W/m^{-2}-μm. The length between the electrodes is ℓ and the photoconductor has depth d_p and width w. By assuming that the photoconductor absorbs the photons impinging upon it with quantum efficiency $\alpha \equiv \alpha(\lambda)$, there will be an increase in equilibrium carrier concentration (per unit wavelength) of

$$n' = \frac{I_\lambda \ell w t_p}{h\nu \ell w d_p} \tag{16a}$$

$$n' = \frac{\alpha \Phi_\lambda t_p}{\ell w d_p} \tag{16b}$$

where Φ_λ is the total number of photons arriving per second. The increase in current in the measuring circuit is then (ref. 5)

$$i' = \frac{q\Phi_\lambda t_p \alpha E \mu w d_p}{\ell w d_p} \tag{17a}$$

$$i' = q\Phi_\lambda \alpha \frac{G_p}{\ell} \tag{17b}$$

where G_p is $E\mu t_p$ and is called the photoconductor gain. The total current generated is then

$$i' = q \int_{\lambda_1}^{\lambda_2} \alpha \Phi_\lambda \frac{G_p}{\ell} \, d\lambda \tag{18}$$

In actual operation the photoconductor is generally operated with constant bias current. Thus an increase in photocurrent is exactly balanced by a decrease in voltage across the photoconductor to hold the current of the total device constant. Detection is therefore by measurement of the photoconductor voltage changes. Proper operation requires that these changes be small in comparison with the dark (nonsignal) bias current and voltage. Such a mode of operation is assumed here.

As mentioned earlier, noise in photoconductors can be divided into three major categories and may be represented as three equivalent noise current generators per $Hz^{1/2}$ (see ref. 6):

$$i_{NT}^2 = \frac{4KTwq\mu n_t' d_p}{\ell} + \frac{4(i' + i_{bias})^2}{\left(\int_{\lambda_1}^{\lambda_2} \alpha \Phi_\lambda \, d\lambda\right)\left[1 + 2\pi f (t_p)^2\right]} + \frac{C'(i' + i_{bias})}{w d_p \ell f} \tag{19}$$

where the first term on the right is Johnson noise, the second is G-R noise, and the third is 1/f noise. For the HCT detector used here, the basic signal-to-noise ratio resulting from dividing equation (18) by equation (19) approaches the value that would be expected for a perfect photoconductor.

The figure of merit which best describes absolute detector performance D^* takes on its maximum value greater than 1×10^{10} cm-$Hz^{1/2}$ per watt at about 12 μm for the HCT detector whereas an ideal photoconductor has a theoretical value of 3×10^{10} cm-$Hz^{1/2}$ per watt at that wavelength.

Preamplifier.- In order not to degrade system performance from that possible with the HCT detector, the signal must be boosted by an extremely low noise preamplifier. This is a difficult requirement since the noise per $Hz^{1/2}$ presented to the preamplifier is an extremely low value. In fact, the voltage noise associated with the detector is not far from that of a resistor generating Johnson noise alone. Evaluating the Johnson noise component of equation (19) gives per $Hz^{1/2}$ a value of 1.0×10^{-9} V for the 40-ohm HCT photoconductor used in this system. If it is assumed that the G-R and 1/f components of noise are near this value, then the preamplifier noise must be less than 1 to 2 nV per $Hz^{1/2}$.

The preamplifier used in this system is a commercial low-noise operational amplifier whose noise figure is specified at 2 dB for a 100-ohm source impedance. Unfortunately, the bias on the detector requires a balancing circuit introducing additional noise. The circuit in figure 7 which represents the detector-preamplifier and balancing circuit can be analyzed to yield the condition for balance, sensitivity to signal variations, and noise.

For low-frequency conditions and typical operating conditions, the performance of the circuit can be approximated by

$$V_o = -V_{BB}\frac{R_f}{R_1} + V_{BB}\left(1 + R_f\frac{R_2 + R_1}{R_2R_1}\right)\frac{\xi_\lambda}{\xi_\lambda + R_B} \tag{20}$$

The condition for balance may be found by setting $V_o = 0$ and solving for R_1:

$$R_1 \approx \frac{R_BR_2}{\xi_\lambda} \tag{21}$$

Using the values for the circuit in this system (R_2 = 50 ohms, R_B = 250 ohms, and ξ_λ = 40.5 ohms) yields a value for R_1 of 308.6 ohms which is close to the measured value of 306 ohms.

Since the preamplifier was supplied with an unknown feedback resistor R_f, measurements were made to determine its value. Resistor R_1 was varied, and the change in output signal was used in conjunction with equation (21) to give R_f = 4880 ohms. This result agrees well with the nominal value (5000 ohms ± 10 percent) given by the manufacturer. Note that equation (20) gives the sensitivity to signal changes; that is,

$$\frac{\partial V_o}{\partial \xi_\lambda} \approx \frac{R_fV_{BB}}{\left(\frac{R_1R_2}{R_1 + R_2}\right)R_B} \tag{22}$$

where it is assumed that $\xi_\lambda \ll R_B$, as is the case.

The effect at the output of the various noise sources can best be arrived at by combining the noise sources by using superposition and root sum of squares per $Hz^{1/2}$

$$v_{NT} = \left\{\left(1 + \frac{R_f}{R_2'}\right)^2\left[v_{NA}^2 \pm \left(\frac{\xi_\lambda}{\xi_\lambda + R_B}\right)^2\left(4kTR_B + i_{NT}^2R_B^2\right)\right]\right.$$

$$\left. + \left(\frac{R_f}{R_2'}\right)^2(4kTR_2') + 4kTR_f\right\}^{1/2} \qquad (23)$$

where

$$R_2' = \frac{R_1R_2}{R_1 + R_2}$$

In equation (19) $\xi_\lambda = \dfrac{\ell}{q\mu n_t' w d_p}$, the detector noise approaches the Johnson noise value over the electrical frequencies of interest, and $\dfrac{R_f}{R_2'} \approx 1 + \dfrac{R_f}{R_2'}$. The following equation thus represents the system output noise voltage per $Hz^{1/2}$:

$$v_{NT} \approx \left[v_{NA}^2 + 4kT\left(\frac{R_B\xi_\lambda}{R_B + \xi_\lambda} + R_2'\right)\right]^{1/2}\frac{R_F}{R_2'} \qquad (24)$$

Values for $\dfrac{R_B\xi_\lambda}{R_B + \xi_\lambda}$ (= 34.48 ohms) and R_2' (= 43.0 ohms) yield (with $v_{NA} = 0$) a noise voltage per $Hz^{1/2}$ of

$$v_{NT} \approx 1.27 \times 10^{-9}\,\frac{R_f}{R_2'} \qquad (25)$$

By assuming that the preamplifier noise figure of 2 dB is correct and that $R_f = 4880$ ohms, one can expect the predicted preamplifier equivalent input noise voltage per $Hz^{1/2}$ of 1.6×10^{-9} volt.

Table II gives measured equivalent input noise voltage obtained for the system with the HCT detector on the one hand and a 41-ohm dummy resistor on the other hand. Note the good agreement of both cases with the above predicted value except at the lower frequencies. The influence of 1/f noise, which has been neglected, can easily explain the increase in noise at lower frequencies and is assumed to be the source of difference between low-frequency noise values and prediction. Since 1/f noise is an empirically determined quantity and not predictable, it is assumed to be defined by these measurements.

The effect of 1/f noise can be taken into account by integrating the function C/f over the frequencies encountered. The value assigned to C is the observed value of 1/f noise at a frequency at which the 1/f is dominant. At a frequency of 5 kHz, the equivalent input noise voltage is 4.3×10^{-9} per $Hz^{1/2}$ or

$$\frac{K}{5 \times 10^3} = (4.3 \times 10^{-9})^2$$

$$K = 9.2 \times 10^{-14}$$

The noise voltage can be determined by integrating the squared noise voltage over the assumed frequency range between 40 Hz and 40 kHz, and taking the square root (assuming for the moment that 1/f is the only noise source). The complete effect of the two dominant noise sources, the white and 1/f components, can be computed with a root-sum-of-squares calculation. The value for the equivalent input 1/f noise is 0.799×10^{-6} V. The value for the equivalent input white noise component in the 40-kHz bandwidth is 0.400 μV. After these noise sources have been assembled, a root-sum-of-squares calculation gives an equivalent input noise voltage of 0.900×10^{-6} V.

Including the approximate preamplifier gain of 115 and a postamplifier gain of G' gives a predigitized noise of $1.035 \times G' \times 10^{-4}$ V.

Signal and Noise Measurements

A calibrated blackbody source positioned 1.02 m from the imager objective lens was set for 800 K and allowed to stabilize for at least 3 hours. A circular aperture 0.87 cm in diameter was placed over the blackbody source. In addition, a known high-pass interference filter covered the aperture of the source to limit the lower wavelength of the radiation to 8 μm. The blackbody source aperture roughly corresponds in diameter to two image elements. Moving the source laterally and vertically positioned the image near the center of the image field to minimize the effect of off-axis aberrations and vignetting. Smaller lateral and vertical positioning was required to locate the image so that it filled one image element uniformly with roughly equal contributions to adjacent image elements.

A predicted value for the signal s_j for the central image element is given by equation (7b), with the values $A_o = 9.133 \times 10^{-4}$ m^2, $\Omega = 1.24 \times 10^{-5}$ sr, $G = 1206$, N_j equivalent to the source radiance of an 800-K extended source, and $\tau_H(\lambda)$ the optics transmissivity. Calculations made by using a table of values for the wavelength dependence of a blackbody source radiance, the optical transmissivity, and detector responsivity give a value for the integral on the right-hand side of equation (7b) of 1.64×10^4. Utilizing the electronic gain gives a predicted signal level for the central pixel of 0.224 V.

An average signal voltage was determined for the central image element by taking the arithmetic mean of 50 measurements. This value was 0.24633 V with a standard deviation of 5.2×10^{-4} V.

Observation of system operation indicated noise in excess of that expected from the detector-preamplifier-digitization process. In order to determine properly the effect of the Hadamard technique on system noise and to compare the noise measurements with prediction, three noise measurements were made. First, actual detector noise measurements after amplification and digitization were taken with the detector removed from the imager. The detector then viewed a 300-K stationary background with emissivity equivalent to that of the mask. Second, noise measurements were taken with the detector replaced in the imager; thus, the rotating mask and the capped lens are viewed. The final noise measurement was taken after processing through the Hadamard inversion by taking an average of the rms noise of 10 image elements. (Fifty measurements of each element were made.) The results are summarized in table III. Excess noise was being generated when the detector viewed the rotating mask. This noise was approximately a factor of three greater than the electronic noise, including quantization noise.

The reduction in system noise was found to be a factor of 14.5 when compared with the system noise before Hadamard processing. Compared with the detector-amplifier-digitization noise, the reduction was only a factor of 5. Thus, the Hadamard process reduced system noise by a factor close to the predicted value of 16 (that is, $m^{1/2}/2$). However, for the particular instrument used in these tests, the system noise was somewhat higher than it should have been. Investigation indicated that vibration in the rather large code wheel was the source of this excess noise. Proper mechanical design should virtually eliminate this problem; therefore, it is not expected to be a basic limitation.

COMPARISON OF EXPERIMENTAL AND THEORETICAL RESULTS

The foregoing analysis and measurement results suggest that four specific signal-to-noise ratio performance values be compared. In addition, the analysis provides a means for generalizing the performance comparison between the Hadamard imager and the conventional imager.

First, the four specific signal-to-noise ratio performance values given for comparison are all for the case of one image element filled by an 800-K extended blackbody source; therefore, all measurements and predictions can be

directly compared. The first of these four values is measured performance for the laboratory Hadamard imager limited by excess noise; the second value is the measured performance of a Hadamard imager limited by detector noise assumed to be reduced by the multiplex factor of 16. A prediction of the best possible Hadamard imager performance is given by the third value. This value, calculated by (1) using equation (7b) and table I to determine the signal and (2) reducing the measured detector noise by assuming a field lens with an effective F number of unity, could be used to minimize the detector area. The fourth value is the best achievable performance with the conventional imaging technique. This fourth value is calculated by dividing the third value by the performance ratio (eq. (13c)), an optical transmissivity of 0.64 for the conventional imager and 0.51 for the Hadamard imager and $F\#_O/F\#_F = 1$ being assumed. A discussion earlier in this paper pointed out that the immersion lens is omitted from the comparison since it could be used with both imaging techniques with the same reduction in detector area.

Comparison of the four values given in table IV reveals that the laboratory Hadamard imager could be improved substantially by eliminating excess noise and by using the minimum possible effective F number field lens. Such improvements would lead to performance approaching that of the conventional imager. This comparison also implies that at best the Hadamard imager can perform no better than a conventional imager when a minimum F number objective lens is used.

The comparison of the two imaging techniques is generalized by using the performance ratio equation repeated here for convenience.

$$PR \approx \frac{\tau_H F\#_O}{2\tau_C F\#_F}$$

An examination of this equation discloses that the Hadamard imaging technique surpasses conventional methods only when the field lens can be a much lower effective F number than the objective lens to more than offset the factor of 2 and the usually slightly lower optical transmissivity of the Hadamard imager. Since the practical minimum F number of the field lens is about 1, a performance advantage is achieved when the objective lens is required to be an F number greater than about 2. For practical systems, this performance advantage is not usually large and does not usually approach the full advantage of $m^{1/2}/2$. For an F/5 imaging objective, an F/1 field lens, and $\tau_H = \tau_C$, for example, the performance advantage would be 2.5.

This performance comparison has considered only signal-to-noise ratio. In practical applications, the two techniques would also be compared for differences in dynamic range requirements, data reduction complexity, mechanical complexity, and cost in determining the relative merits of the two imaging techniques.

CONCLUDING REMARKS

The Hadamard imaging technique was described, and an analysis of its signal-to-noise ratio performance was presented. An expression was derived for comparing potential Hadamard performance with conventional imaging techniques. The optical and electronics subsystems of a laboratory Hadamard imager operating in the thermal infrared spectral region were analyzed, and the signal-to-noise ratio performance of the imager was measured.

The general comparison of Hadamard and conventional imaging was based on a performance ratio which predicts a performance advantage proportional to the F number of the imaging objective lens, rather than the higher performance advantage usually given as one-half the square root of the number of image elements. This significantly lower advantage results because the practical minimum detector size (and noise) is much larger than that required for the conventional imager. In addition, the potential advantage is offset further by a factor of 2 associated with the encoding mask and slightly lower optical transmissivity for the Hadamard imager. Consequently, a performance advantage can be realized only when an F number greater than about 2 is required for the imaging objective lens.

Performance measurements of a laboratory Hadamard imager with a fast objective lens (about F/1) confirmed predictions for the Hadamard imager. Although this particular imager was limited by excess noise caused by a vibration of the rotating mask, the pure detector noise was measured separately to determine potential system performance. In addition, the signal produced by a blackbody source was measured to determine absolute system responsivity, and the noise reduction property of Hadamard imaging was verified.

Results of the general comparison, supported by the laboratory measurements, imply that Hadamard imaging will be useful primarily when design considerations dictate the use of a slow F number objective lens for imaging.

Langley Research Center
National Aeronautics and Space Administration
Hampton, VA 23665
December 20, 1976

REFERENCES

1. Decker, J. A., Jr.: Hadamard-Transform Image Scanning. Appl. Opt., vol. 9, no. 6, June 1970, pp. 1392-1395.

2. Sloane, N. J. A.; Fine, T.; Phillips, P. G.; and Harwit, M.: Codes for Multiplex Spectrometry. Appl. Opt., vol. 8, no. 10, Oct. 1969, pp. 2103-2106.

3. Nelson, E. D.; and Fredman, M. L.: Hadamard Spectroscopy. J. Opt. Soc. America, vol. 60, no. 12, Dec. 1970, pp. 1664-1669.

4. Rose, A.: Noise Currents. Photoelectronic Materials and Devices, Simon Larach, ed., D. van Nostrand Co., Inc., c.1965, pp. 222-238.

5. Bube, Richard H.: Photoconductors. Photoelectronic Materials and Devices, Simon Larach, ed., D. van Nostrand Co., Inc., c.1965, pp. 100-138.

6. Humphrey, James N.: Optimum Utilization of Lead Sulfide Infrared Detectors Under Diverse Operating Conditions. Appl. Opt., vol. 4, no. 6, June 1965, pp. 665-676.

TABLE I.- HADAMARD IMAGER PARAMETERS

Objective lens:	
Aperture diameter, D_o, cm	3.41
Focal length, F_o, cm	3.81
In-focus object distance, L_o, cm	102.20
Image distance, l_o, cm	3.96
Assumed transmissivity	0.85
Encoding mask:	
Elemental solid angle, Ω, sr	1.24×10^{-5}
Height and width of element, H_e and W_e, cm	1.39×10^{-2}
Field stop:	
Height, cm	0.534
Width, cm	0.568
Angular vertical field, deg	7.26
Angular horizontal field, deg	7.72
Field lens:	
Aperture diameter, D_F, cm	1.25
Focal length, F_F, cm	1.25
In-focus object distance, L_F, cm	4.72
Image distance, l_F, cm	1.72
Assumed transmissivity	0.85
Immersion lens:	
Index of refraction at 10 μm, n	4.005
Detector (HCT):	
Length of one side, w, cm	0.25
Peak responsivity of immersed detector at 11 μm, V/W	26.9
Other:	
Mask to field stop distance, x, cm	0.25
Field stop to field lens distance, y, cm	0.513
Image diameter after immersion, d_H, cm	0.307
Assumed loss due to circular image overfilling square detector	0.82
Peak transmissivity at 9 μm of 8.0-μm cutoff filter	0.88

TABLE II.- COMPARISON OF PREDICTION AND EXPERIMENT FOR PREAMPLIFIER INPUT NOISE VOLTAGE WITH V_{BB} = 10.0 VOLTS

Frequency, kHz	Predicted noise voltage, $V/Hz^{1/2}$	Measured noise voltage, $V/Hz^{1/2}$, of -	
		41-ohm resistor	HCT detector
5	1.60×10^{-9}	4.3×10^{-9}	4.3×10^{-9}
10	1.60	3.3	3.3
15	1.60	2.5	3.0
20	1.60	2.5	2.5
25	1.60	2.15	2.5
30	1.60	2.15	2.17
35	1.60	2.15	2.17
40	1.60	2.15	2.0
45	1.60	1.6	2.0
50	1.60	1.6	1.9

TABLE III.- NOISE MEASUREMENT RESULTS

	Root-mean-square noise voltage, volts
Detector-preamplifier noise before matrix inversion	2.24×10^{-3}
System noise before matrix inversion	6.75×10^{-3}
Noise after matrix inversion	4.62×10^{-4}

TABLE IV.- PERFORMANCE COMPARISON

	Signal-to-noise ratio (800-K source)
Measured for system-noise-limited Hadamard imager	530
Measured for detector-noise-limited Hadamard imager	1600
Predicted for Hadamard imager with minimum detector area	2200
Predicted for conventional imager with equivalent objective lens and image element size	5300

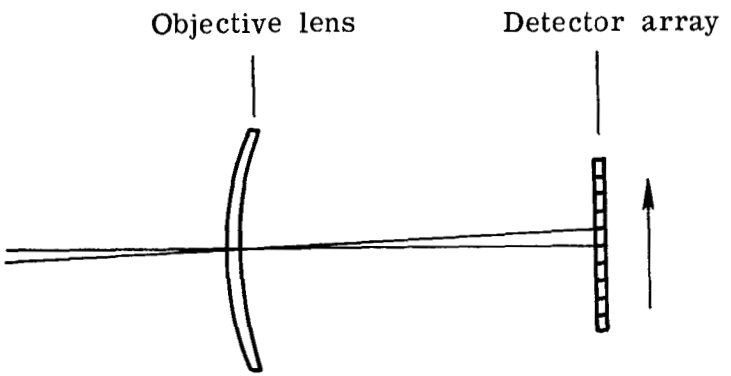

(a) Detector array for electronic scanning.

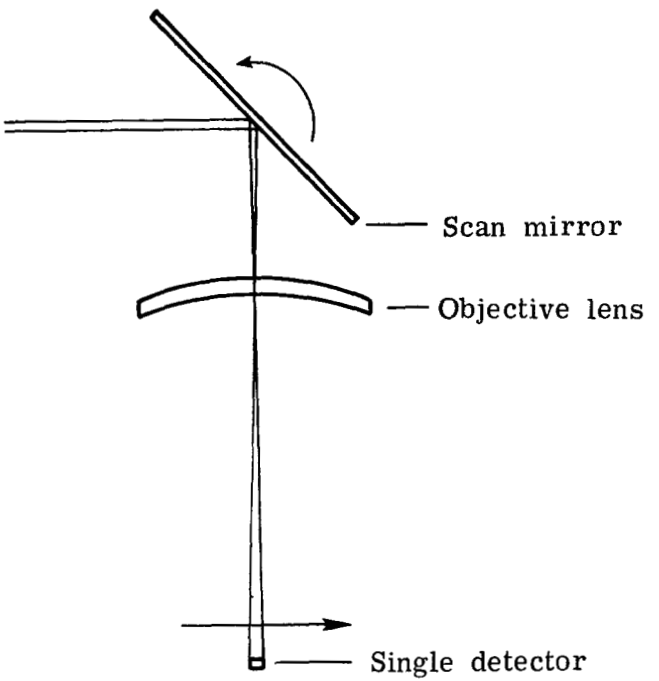

(b) Scan mirror/single detector combination for mechanical scanning.

Figure 1.- Conventional imager.

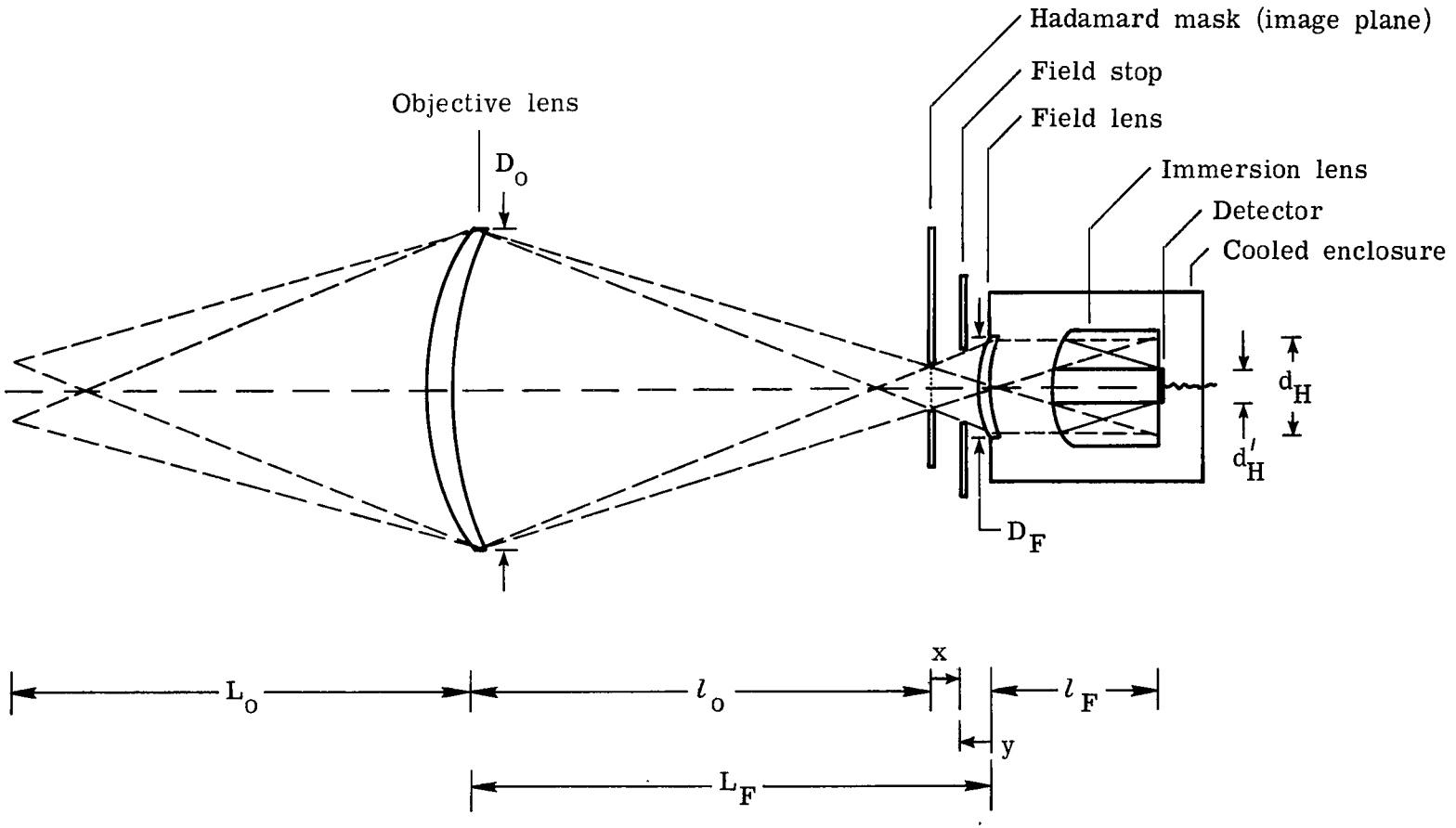

Figure 2.- Hadamard imager optical subsystem.

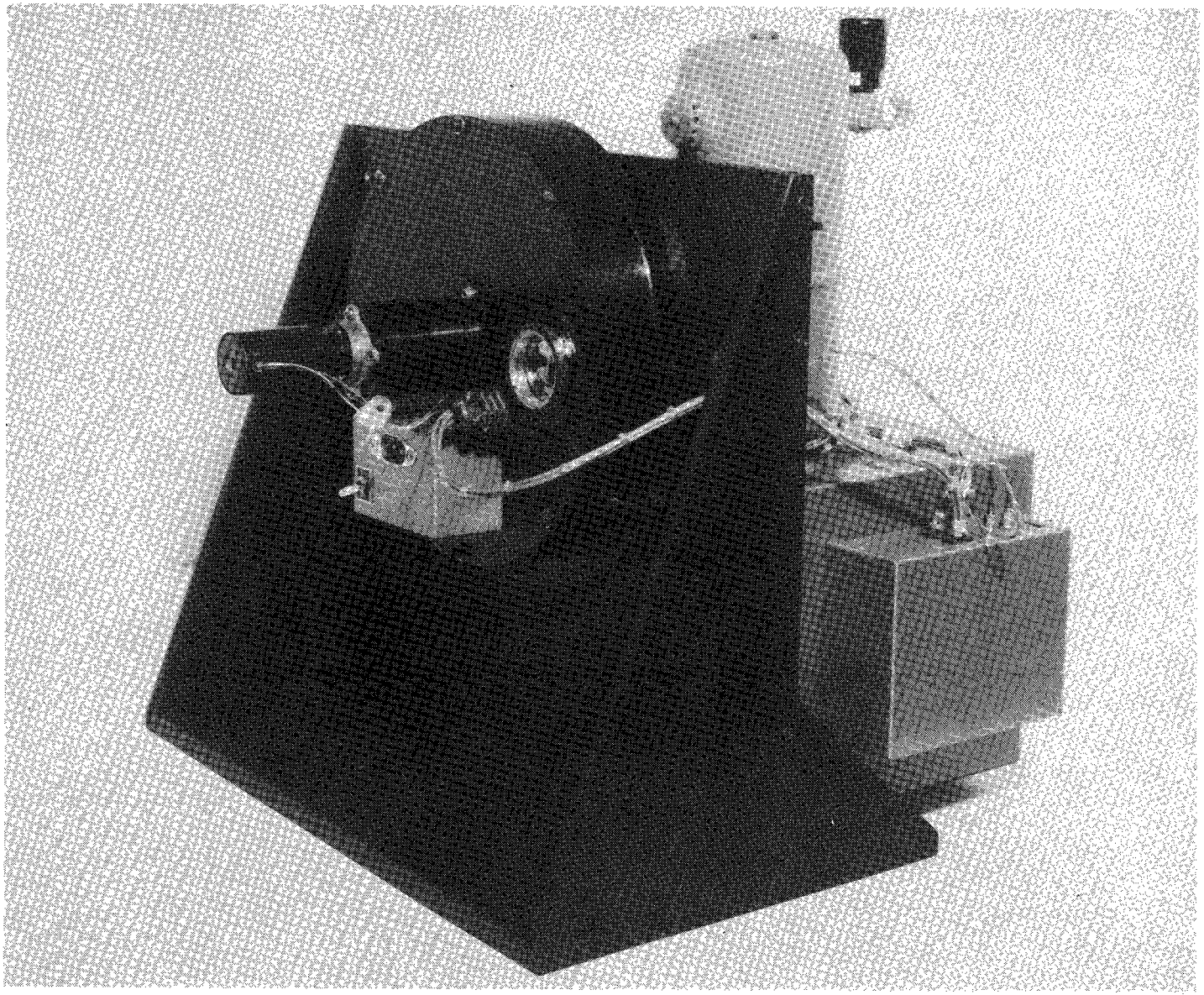

L-76-7129

Figure 3.- Photograph of Hadamard imager.

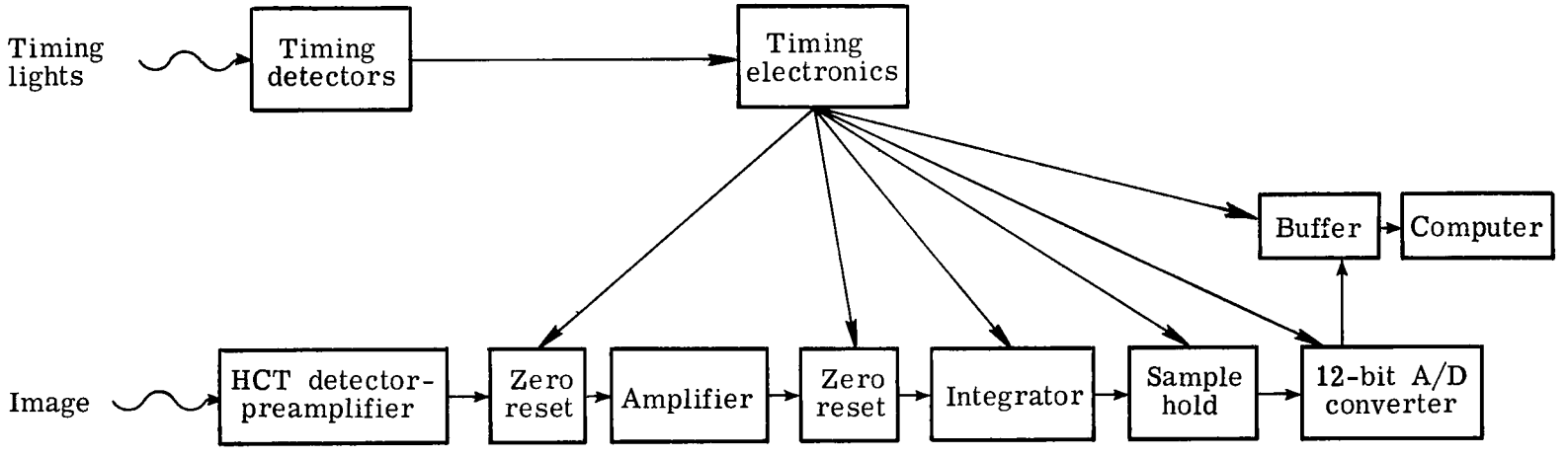

Figure 4.- Block diagram of electronics subsystem.

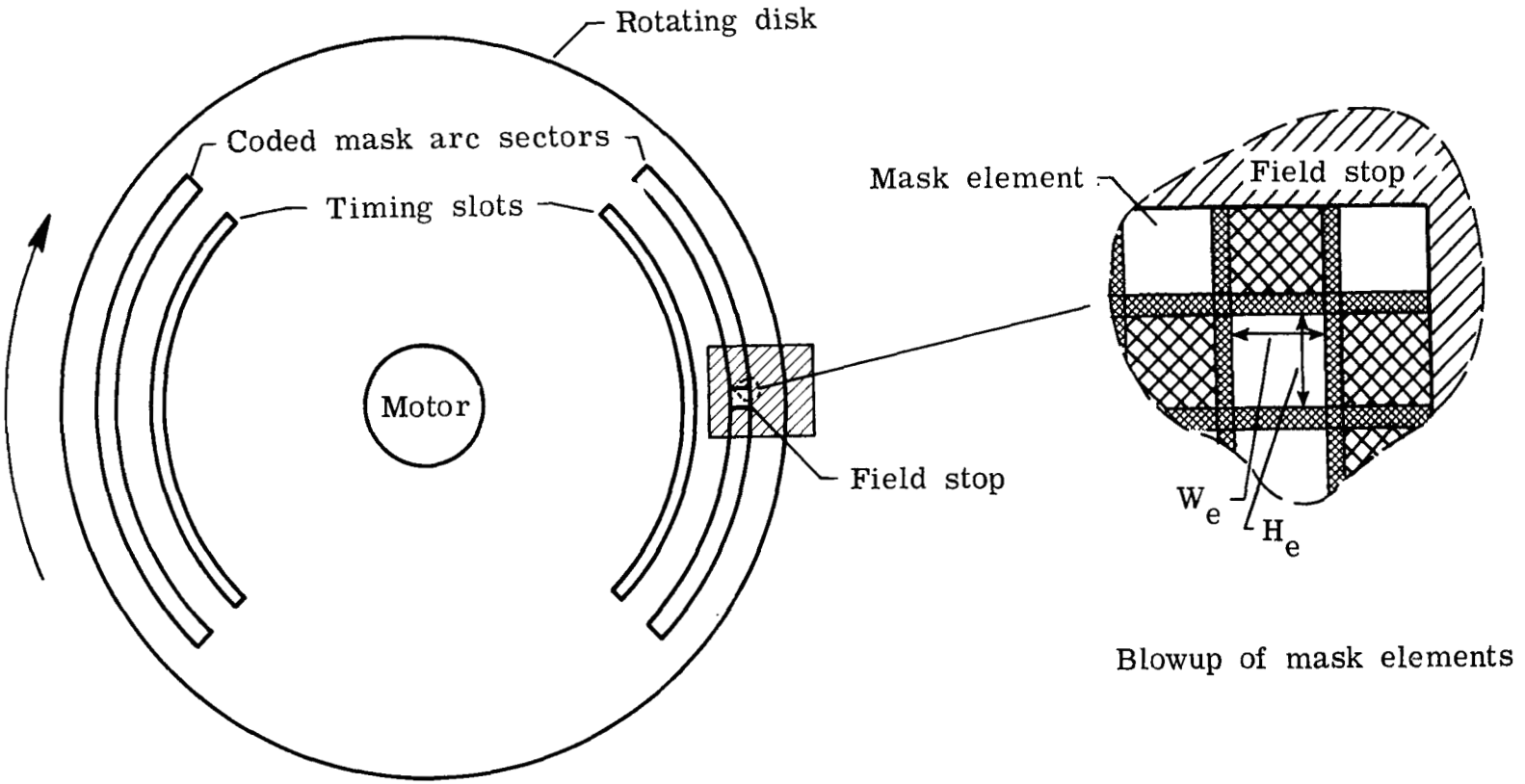

Figure 5.- Diagram of rotating disk containing mask code and timing slots.

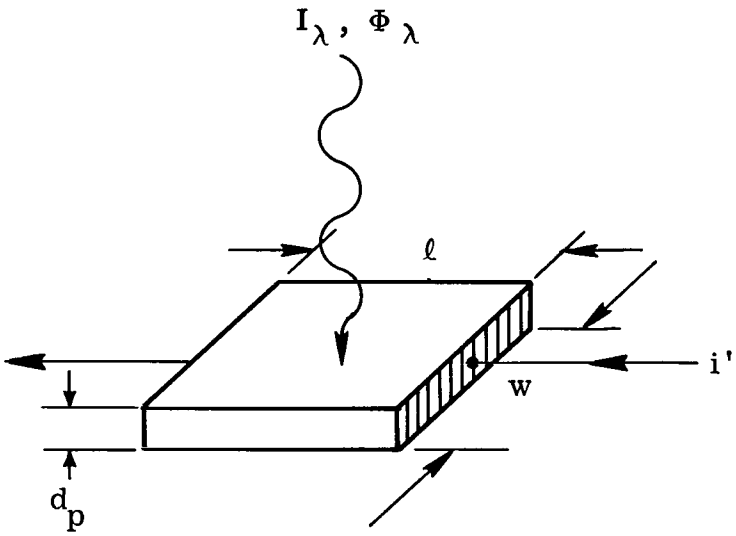

Figure 6.- Photoconductor geometry.

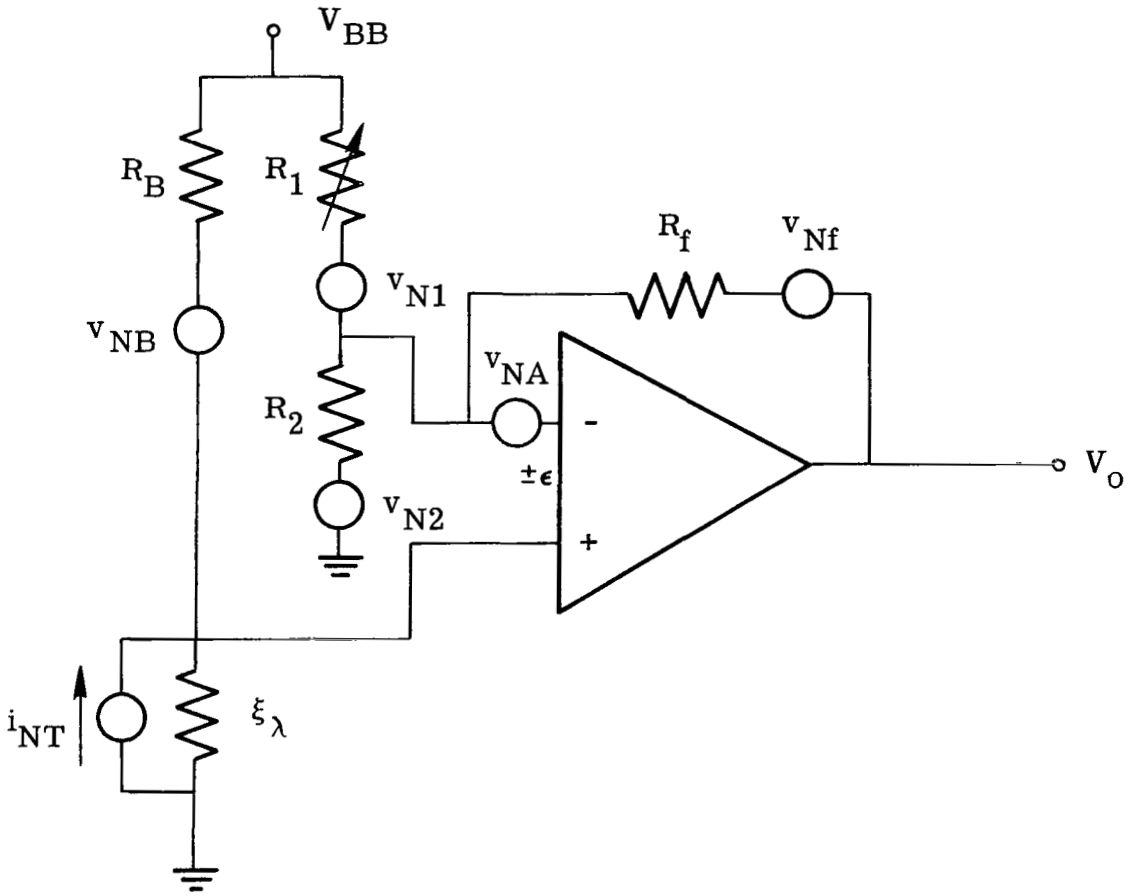

Figure 7.- Photoconductor, preamplifier, and balancing circuit (including prominent noise sources).

NATIONAL AERONAUTICS AND SPACE ADMINISTRATION
WASHINGTON, D.C. 20546

OFFICIAL BUSINESS
PENALTY FOR PRIVATE USE $300

SPECIAL FOURTH-CLASS RATE BOOK

POSTAGE AND FEES PAID
NATIONAL AERONAUTICS AND SPACE ADMINISTRATION
451

U.S.MAIL

132 001 C1 U D 770211 S00903DS
DEPT OF THE AIR FORCE
AF WEAPONS LABORATORY
ATTN: TECHNICAL LIBRARY (SUL)
KIRTLAND AFB NM 87117

If Undeliverable (Section 158 Postal Manual) Do Not Return

"The aeronautical and space activities of the United States shall be conducted so as to contribute . . . to the expansion of human knowledge of phenomena in the atmosphere and space. The Administration shall provide for the widest practicable and appropriate dissemination of information concerning its activities and the results thereof."

—NATIONAL AERONAUTICS AND SPACE ACT OF 1958

NASA SCIENTIFIC AND TECHNICAL PUBLICATIONS

TECHNICAL REPORTS: Scientific and technical information considered important, complete, and a lasting contribution to existing knowledge.

TECHNICAL NOTES: Information less broad in scope but nevertheless of importance as a contribution to existing knowledge.

TECHNICAL MEMORANDUMS: Information receiving limited distribution because of preliminary data, security classification, or other reasons. Also includes conference proceedings with either limited or unlimited distribution.

CONTRACTOR REPORTS: Scientific and technical information generated under a NASA contract or grant and considered an important contribution to existing knowledge.

TECHNICAL TRANSLATIONS: Information published in a foreign language considered to merit NASA distribution in English.

SPECIAL PUBLICATIONS: Information derived from or of value to NASA activities. Publications include final reports of major projects, monographs, data compilations, handbooks, sourcebooks, and special bibliographies.

TECHNOLOGY UTILIZATION PUBLICATIONS: Information on technology used by NASA that may be of particular interest in commercial and other non-aerospace applications. Publications include Tech Briefs, Technology Utilization Reports and Technology Surveys.

Details on the availability of these publications may be obtained from:

SCIENTIFIC AND TECHNICAL INFORMATION OFFICE

NATIONAL AERONAUTICS AND SPACE ADMINISTRATION

Washington, D.C. 20546